

The impact of rain to observed signal from Chinese Gaofen-3 synthetic aperture radar in typhoons

Jian Shi¹, Jiachen Hu², Weizeng Shao^{2*}, Xiaoqing Wang³, Xinzhe Yuan⁴, Liangbo Zhao⁵, Xiaofeng Li²

¹ College of Meteorology and Oceanography, National University of Defense Technology, Nanjing 211101, China

² Marine Science and Technology College, Zhejiang Ocean University, Zhoushan 316022, China

³ School of Electronics and Communication Engineering, Sun Yat-sen University, Guangzhou 510275, China

⁴ Key Laboratory of Space Ocean Remote Sensing and Application, National Satellite Ocean Application Service, Beijing 100081, China

⁵ Institute of Spacecraft System Engineering, China Academy of Space Technology, Beijing 100094, China

Received 28 May 2019; accepted 2 September 2019

© Chinese Society for Oceanography and Springer-Verlag GmbH Germany, part of Springer Nature 2019

Abstract

Gaofen-3 (GF-3), a Chinese civil synthetic aperture radar (SAR) at C-band, has operated since August 2016. Remarkably, several typhoons have been captured by GF-3 around the China Seas over its last two-year mission. In this study, six images acquired in Global Observation (GLO) and Wide ScanSAR (WSC) modes at vertical-vertical (VV) polarization channel are discussed. This work focuses on investigating the observation of rainfall using GF-3 SAR. These images were collocated with winds from the European Centre for Medium-Range Weather Forecasts (ECMWF), significant wave height simulated from the WAVEWATCH-III (WW3) model, sea surface currents from climate forecast system version 2 (CFSv2) of the National Centers for Environmental Prediction (NCEP) and rain rate data from the Tropical Rainfall Measuring Mission (TRMM) satellite. Sea surface roughness, was compared with the normalized radar cross section (NRCS) from SAR observations, and indicated a 0.8 correlation (COR). We analyzed the dependences of the difference between model-simulated NRCS and SAR-measured NRCS on the TRMM rain rate and WW3-simulated significant wave height. It was found that the effects of rain on SAR damps the radar signal at incidence angles ranging from 15° to 30°, while it enhances the radar signal at incidence angles ranging from 30° to 45° and incidence angles smaller than 10°. This behavior is consistent with previous studies and an algorithm for rain rate retrieval is anticipated for GF-3 SAR.

Key words: Gaofen-3, synthetic aperture radar, typhoon

Citation: Shi Jian, Hu Jiachen, Shao Weizeng, Wang Xiaoqing, Yuan Xinzhe, Zhao Liangbo, Li Xiaofeng. 2019. The impact of rain to observed signal from Chinese Gaofen-3 synthetic aperture radar in typhoons. *Acta Oceanologica Sinica*, 38(11): 121–133, doi: 10.1007/s13131-019-1502-7

1 Introduction

Typhoons are a natural disaster in coastal areas, and in particular, rainfall is always accompanied with strong winds. The track and category of a typhoon can be monitored by means of passive optical satellites, e.g., moderate-resolution imaging spectroradiometer (MODIS) of Earth Observation System (EOS). However, sea surface information is undetectable by optical satellite due to the cloud layer in a typhoon or hurricane. Synthetic aperture radar (SAR) is an active sensor operating at the microwave band, which has the ability to detect the sea surface in day-time under extreme conditions. Therefore, SAR is an advanced technique for typhoon monitoring, especially for heavy rainfall (Atlas, 1994; Weinman et al., 2009).

Satellites carrying C-band (5.3 GHz) SAR sensors include ERS-1/2, ENVISAT-ASAR, RADARSAT-1/2 (R-1/2) and Sentinel-1A/1B (S-1) and Gaofen-3 (GF-3). GF-3 was launched by the China Academy of Space Technology (CAST) in August 2016, and

is the first civilian SAR to have a 755-km orbit height above the earth's surface with a 26-d repeat cycle. GF-3 operates in 12 imaging modes with a fine spatial resolution of up to 1 m. In particular, the images acquired in Global Observation (GLO) and Wide ScanSAR (WSC) modes have the capability of observing typhoons with a swath coverage larger than 400 km. Recently, marine applications using GF-3 SAR data have performed well in wind (Ren et al., 2017; Wang et al., 2018; Shao et al., 2019) and wave monitoring (Shao et al., 2017a; Zhu et al., 2019). In particular, algorithms for typhoon wind and wave retrieval using GF-3 data acquired in GLO and WSC mode have been previously studied (Shao et al., 2018; Ji et al., 2018).

The SAR-measured normalized radar cross section (NRCS) over the sea surface is mainly determined by wind-driven gravity-capillary waves due to Bragg scattering. At present, rainfall event monitoring is an interesting topic for the SAR remote sensing community. It is well known that the rain-induced backscatter-

Foundation item: The Fundamental Research Funds for Zhejiang Provincial Universities and Research Institutes under contract No. 2019J00010; the National Key Research and Development Program of China under contract No. 2017YFA0604901; the National Natural Science Foundation of China under contract Nos 41806005, 41676014 and 41776183; the Public Welfare Technical Applied Research Project of Zhejiang Province of China under contract No. LGF19D060003; the Science and Technology Project of Zhoushan City under contract No. 2019C21008.

*Corresponding author, E-mail: shaoweizeng@zjou.edu.cn

ing signal includes two aspects: (1) atmospheric effects, e.g., attenuation and backscattering, and modification of backscattering by falling raindrops over the sea surface, which directly degrade the accuracy of a scatterometer (Daper and Long, 2004; Allen and Long, 2005) and SAR (Melsheimer et al., 1998; Nie and Long, 2008), and (2) wind retrieval due to NRCS which is linearly related with wind speed (Masuko et al., 1986). Rain-induced effects in sea surface regions include, turbulence or damping, splash products and down-draft (Lin et al., 2001).

Based on multi-frequency SIR-C/X-SAR data and ERS-1/2 SAR data, Melsheimer et al. (2001) demonstrated that the effect of rainfall on a SAR backscattering signal is generally reduced at low incidence angles and the signal is enhanced at high incidence angles. The wave damping effect induced by rain, which depends on many factors, e.g., the type of rain, rain rate, drop size distribution and incidence angle, is relatively weak because surface turbulence is under-developed at the beginning of a rain event. The damping effect increases along with the continuous rain event then gets attenuated after the rain moves on. Moreover, the damping effect might last for a long period of time even after the end of a rain event, since the turbulence decays slowly due to the molecular viscosity of sea water and the strength of the mixing turbulent layer (Hallett and Christensen, 1984; Nystuen and Jeffrey, 1990). The sea surface roughness from falling raindrops generates various splash products including ring wave, stalk, and crown, and mainly depends on the modification of the wavelength of a wind-induced sea surface wave (Nie and Long, 2007; Fritz and Chandrasekar, 2012; Xu et al., 2015), possibly due to rain increasing or decreasing the amplitude of the wind-induced Bragg waves. Although these splash products contribute to the backscattering signal, the ring wave is found to be the dominant feature at the co-polarization polarization channel (Alpers et al., 2007). In addition to the backscattering effect induced by raindrops, sea surface roughness is also influenced by the down-draft associated with a rain event and large-scale wind flow (Zhang et al., 2016).

During the past two-year mission of C-band GF-3, several typhoons were captured around the China Seas. These vertical-vertical (VV) polarization images ranged from 10° to 45° and so provide a good opportunity to study the effects of rain ratio on SAR measurements at different incidence angles and wind speeds under extreme sea states. We organize the remaining parts of this paper as follows: a description of the data collections, including SAR images, wind and wave from the European Centre for Medium-Range Weather Forecasts (ECMWF), significant wave height simulated from the WAVEWATCH-III (WW3) model, sea surface current from the climate forecast system version 2 (CFSv2) of the National Centers for Environmental Prediction (NCEP) and rainfall from the Tropical Rainfall Measuring Mission (TRMM) satellite, is presented in Section 2. The methodology for sea surface roughness simulation of SAR is introduced and the simulated results are compared with the observations from GF-3 SAR in Section 3. The analysis of rain on GF-3 SAR at various conditions is exhibited in Section 4 and the discussions are presented in Section 5. The conclusions are summarized in Section 6.

2 Description of dataset

In this study, a total six GF-3 SAR images are available, in which the typhoon eyes can be clearly observed. These images have a larger than 100 m pixel size for GF-3 SAR acquired in GLO and WSC mode with a swath coverage of more than 400 km, and were processed to a Level-1B (L-1B) product during Typhoons

Noru, Dokuri, Talim, Hato and Jongdari, when the maximum wind speed reached 50 m/s. The calibrated quick-look images of the SAR images are shown in Fig. 1, on which are overlaid the tracks of typhoons provided by the Japan Meteorological Agency (JMA) and the Lines A–D represent the meshes passing the typhoon eyes. Brief descriptions of these six images and information about the corresponding typhoons are listed in Table 1. The following equation is employed to obtain the NRCS of VV-polarization GF-3 SAR acquired in L-1B mode.

$$\sigma^0 = DN^2 \left(\frac{M}{65\ 535} \right)^2 - N, \quad (1)$$

where σ^0 is the calibration NRCS with unit of dB, DN is the SAR-measured intensity, M is the external calibration factor and N is the offset constant stored in the annotation file.

Since 1979, the ECMWF has provided a world-wide open access dataset, including global atmospheric and marine products with a fine spatial resolution of 0.125°×0.125° (approximately 12.5 km×12.5 km) at intervals of 6 hours. At present, ECMWF reanalysis data are popularly used for the development of SAR wind retrieval algorithms, e.g., geophysical model function (GMF) at C-band CMOD5 (Hersbach et al., 2007) and CMOD5N (Hersbach, 2010), and SAR wave retrieval algorithms at C-band (Sheng et al., 2018) and X-band (Shao et al., 2017b). Although we also employ the ECMWF wind data at a 0.125° grid in typhoons, the gridded data is bilinearly interpolated in temporal scale because there is a time difference between the SAR images and the ECMWF interval data. The ECMWF winds are the forcing field in the simulation of the WW3 model and the validation of simulated significant wave height corresponding to the typhoon images has been previously presented in Ji et al. (2018), therefore, we do not repeat it here. The WW3-simulated wave map at a 0.1° grid is shown in Fig. 2, in which the rectangles represent the spatial coverage of six images. The effect of rain can be observed in Fig. 1, e.g., the black spiral moves away from the typhoon eyes on the GF-3 SAR images. Therefore, the rainfall rate data measured by the TRMM satellite at intervals of 3 h with a spatial resolution of 0.25°×0.25° were collected as the additional data, which is a popular method for studying the climatology of the tropical precipitation variability (Kim and Alexander, 2013). It was necessary to establish a time difference of less than 1.5 h between the SAR imaging time and the TRMM data. The TRMM rain rate maps with up to 20 mm/h corresponding to the six images are shown in Fig. 3.

Because the SAR backscattering signal at the VV-polarization channel encounters a saturation problem at strong winds (probably greater than 20 m/s) (Hwang et al., 2010; Voronovich and Zavorotny, 2014, the widely-used CMOD family, e.g., CMOD5 and CMOD5N, is not suitable for simulating the NRCS in typhoons. A strong wind-induced current plays an important role in typhoon conditions and is a critical issue in using a forecast wave numeric model (Cui et al., 2012). Therefore, we collected the NCEP CFSv2 open-access current data from the National Center of Atmosphere Research (NCAR), which has a 0.5°×0.5° grid at an interval of 6 h. As well, the CFSv2 current data are also bilinearly interpolated in temporal scale in order to matchup with the GF-3 SAR images. In this study, the CFSv2 current vector together with the ECMWF wind vector are used for simulating the NRCS of GF-3 SAR through a parametric backscattering model. The CFSv2 current maps corresponding to the six images are shown in Fig. 4.

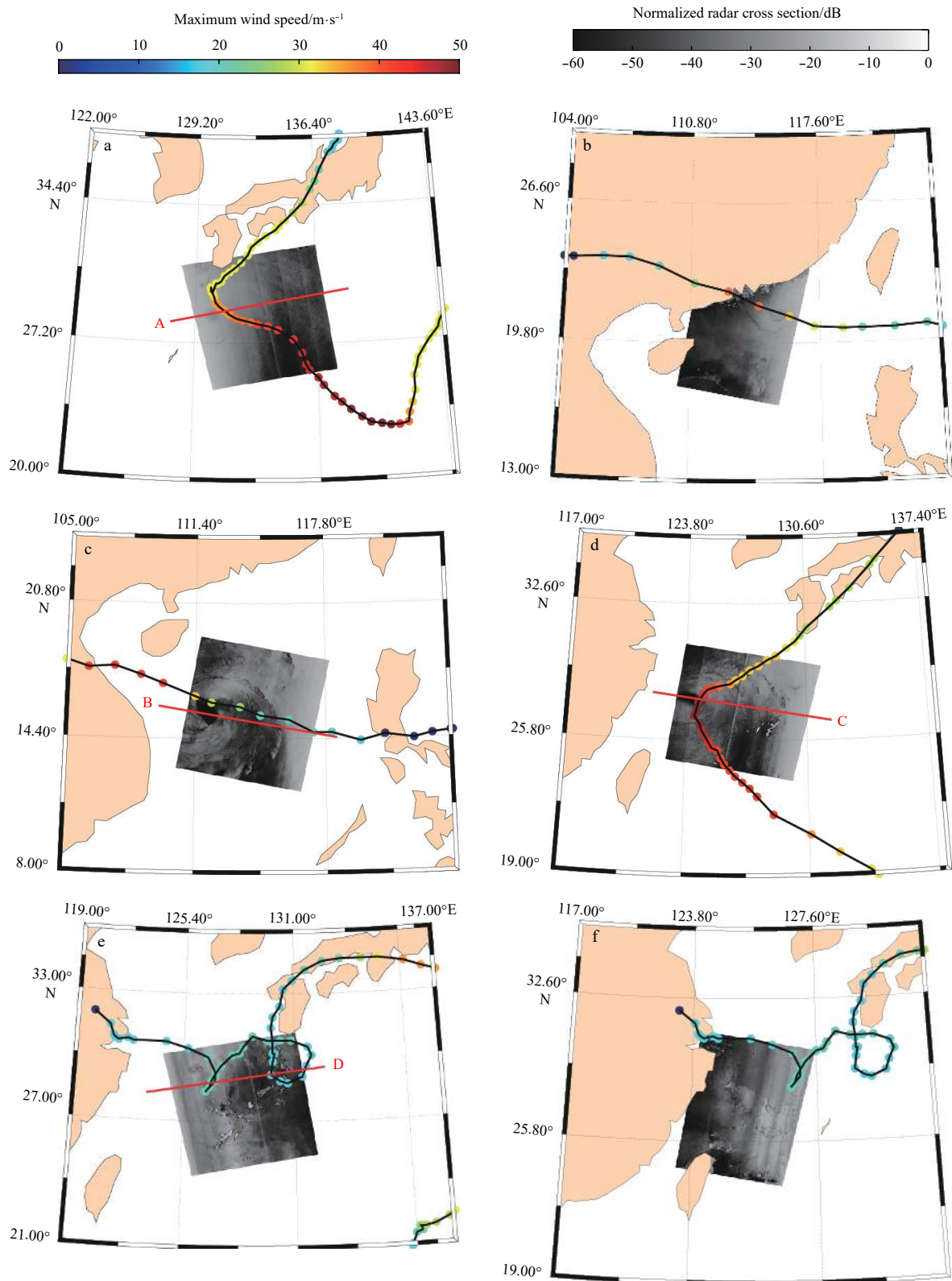


Fig. 1. The quick-look images of six GF-3 SAR images in VV-polarization overlaying the tracks of cyclones. a. The image for Typhoon Noru acquired in Global Observation (GLO) mode on August 04, 2017 at 09:12 Universal Time Coordinated (UTC); b. the image for Typhoon Hato acquired in Wide ScanSAR (WSC) mode on August 22, 2017 at 22:23 UTC; c. the image for Typhoon Doksuri acquired in WSC mode on September 13, 2017 at 22:14 UTC; d. the image for Typhoon Talim acquired in GLO mode on September 14, 2017 at 21:29 UTC; e. the image for Typhoon Jongdari acquired in interferometric WSC mode on August 1, 2018 at 09:34 UTC; and f. the image for Typhoon Jongdari acquired in EW mode on August 1, 2018 at 21:47 UTC.

Table 1. Information from collected GF-3 synthetic aperture radar (SAR) images and corresponding typhoons

Typhoon ID	Acquisition time (YY-MM-DD)	Position of typhoon eye	Incidence angle/(°)	Imaging mode	Pixel size azimuth×range/m
Noru	2017-08-04	28.4°N, 131.4°E	13.1–45.6	GLO	500×500
Hato	2017-08-22	20.8°N, 117.1°E	14.2–41.2	WSC	100×100
Doksuri	2017-09-13	15.8°N, 114.3°E	20.5–43.8	WSC	100×100
Talim	2017-09-14	27.4°N, 124.3°E	14.2–45.8	GLO	500×500
Jongdari	2018-08-01 (am)	30.4°N, 128.0°E	23.1–50.7	WSC	100×100
Jongdari	2018-08-01(pm)	30.3°N, 127.8°E	15.9–47.4	WSC	100×100

3 Methodology

In this section, we first present the methodology for sea surface roughness simulation of SAR based on using the ECMWF wind and CFSv2 current data without considering the rainfall term. Then the simulated NRCSs are compared with the observations from the GF-3 SAR images in order to verify the availability of data.

3.1 Method for simulating NRCS of SAR

In this work, we use the three-scale radar backscattering model based on second order scattering to simulate ocean backscattering. This model combines the advantage of the three-scale model proposed by Romeiser et al. (1997) and the stochastic multiscale model proposed by Plant (2002). Compared with most of the other theoretical ocean scatter models, this model has wider application conditions, and in most cases the simulation error is within 2–3 dB.

In this model, the relationship between the average NRCS and the sea surface wave height autocorrelation function is as follows

$$\sigma_{qp} = \frac{k^2}{4\pi} \exp[-4\varphi(0)k_z^2] |\Gamma_{qp}|^2 \int \exp[-2ik_H \cdot x] \times \{\exp[4k_z^2 \varphi(x)] - 1\} dx, \quad (2)$$

where p and q are the polarization direction of transmission and reception, k is the wavenumber of electromagnetic wave, x is the horizontal coordinate vector, k_H is the horizontal component of the transmitted wavenumber vector, and k_z is the vertical component of the transmitting and receiving electro-magnetic wavenumber. Γ_{qp} is the polarization factor. The coefficient $\varphi(x)$ is the autocorrelation function of wave height.

$$\varphi(x) = \int W(k) \exp(ik \cdot x) dk, \quad (3)$$

where $W(k)$ is the wave spectrum, $\varphi(x)$ reaches the maximum value when $x=0$, that is, the mean square height of the sea surface wave height.

When $(k_{sz} - k_z)^2 \varphi(0) > 10$, the NRCS can be simplified as

$$\sigma_I \approx \frac{k^2 |f_{qp}|^2}{4k_z \sqrt{S_{xx} + S_{yy} - S_{xy}}} \times \exp\left\{-\left[S_{xx}k_x^2 + S_{yy}k_y^2 - \frac{S_{xy}k_x k_y}{\frac{2k_z^2}{(S_{xx} + S_{yy} - S_{xy})}}\right]\right\}, \quad (4)$$

where $S_{xx} = \int W(k) (k\hat{x})^2 dk$, $S_{yy} = \int W(k) (k\hat{y})^2 dk$, $S_{xy} = \int W(k) (k\hat{x})(k\hat{y}) dk$.

When $(k_{sz} - k_z)^2 \varphi(0) < 0.1$, NRCS can be simplified to the Bragg scattering form as follows:

$$\sigma_{qp} \approx 4\pi k^2 |\Gamma_{qp}|^2 k_z^2 W(k_H - k_{sH}). \quad (5)$$

The direct computation of formula (2) is very time consuming. Therefore, it needs to be simplified by using Eqs (4) and (5). The sea surface wave spectrum is divided into three parts: large, medium and small.

$$\begin{aligned} \varphi(x) &= \int_{k_l \geq |k|} W(k) \exp(ik \cdot x) dk + \int_{k_s > |k| > k_l} W(k) \times \\ &\quad \exp(ik \cdot x) dk + \int_{|k| \geq k_s} W(k) \exp(ik \cdot x) dk \\ &= \varphi_l(x) + \varphi_i(x) + \varphi_s(x). \end{aligned} \quad (6)$$

The wave number division scale k_s and k_l satisfy

$$4k_z^2 \varphi_l(0) = 10, \quad (7)$$

$$4k_z^2 \varphi_s(0) = 0.1. \quad (8)$$

The integral term of the Eq. (2) is divided into three parts

$$\sigma_{qp} = \sigma_{qp}^l + \sigma_{qp}^i + \sigma_{qp}^s, \quad (9)$$

where

$$\begin{aligned} \sigma_I &\approx \exp\left\{-(k_{sz} - k_z)^2 [\varphi_i(0) + \varphi_s(0)]\right\} \frac{k^2 |f_{qp}|^2}{2(k_{sz} - k_z) \sqrt{S_{xx} + S_{yy} - S_{xy}}} \times \\ &\quad \exp\left\{-\left[S_{xx}(k_{sx} - k_x)^2 + S_{yy}(k_{sy} - k_y)^2 - \frac{S_{xy}(k_{sx} - k_x)(k_{sy} - k_y)}{\frac{2(k_{sz} - k_z)^2}{(S_{xx} + S_{yy} - S_{xy})}}\right]\right\}, \\ \sigma_{qp}^i &= \frac{k^2}{4\pi} \exp\left[-\varphi_s(0)(k_{sz} - k_z)^2\right] |\Gamma_{qp}|^2 \int \exp[j(k_{sH} - k_H) \cdot x] \times \\ &\quad \exp\left\{(k_{sz} - k_z)^2 [\varphi_i(x) - \varphi_i(0)]\right\} dx, \\ \sigma_{qp} &\approx \pi k^2 |\Gamma_{qp}|^2 (k_{sz} - k_z)^2 W(k_H - k_{sH}). \end{aligned}$$

The above derivation is based on a Gaussian distribution, but the sea surface does not conform to a Gaussian random distribution, the evidence for which is that the scattering intensity in the downwind and upwind incidence angle is different. One solution is to consider the influence of the higher order spectrum of the sea surface in the scattering model. Although this method is relatively strict mathematically, at present, it produces no recognized result for the measurement of the high-order spectrum of the sea surface. Moreover, this method cannot simulate the textural information of sea surface scattering, so it is not widely

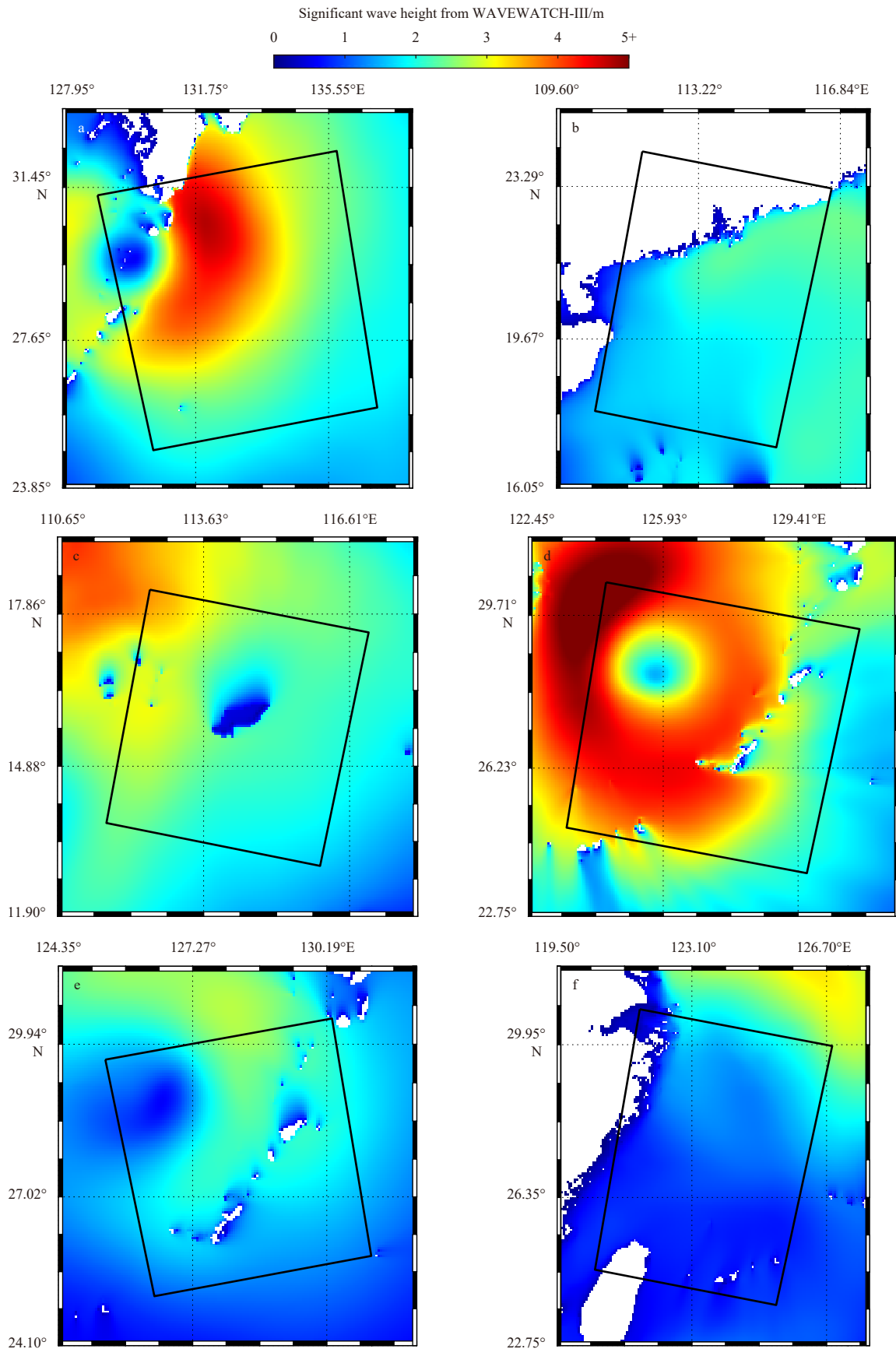


Fig. 2. The significant wave height current maps simulated from the WAVEWATCH-III (WW3) model, in which the black rectangles correspond to the spatial coverage of six GF-3SAR images as shown in Fig. 1.

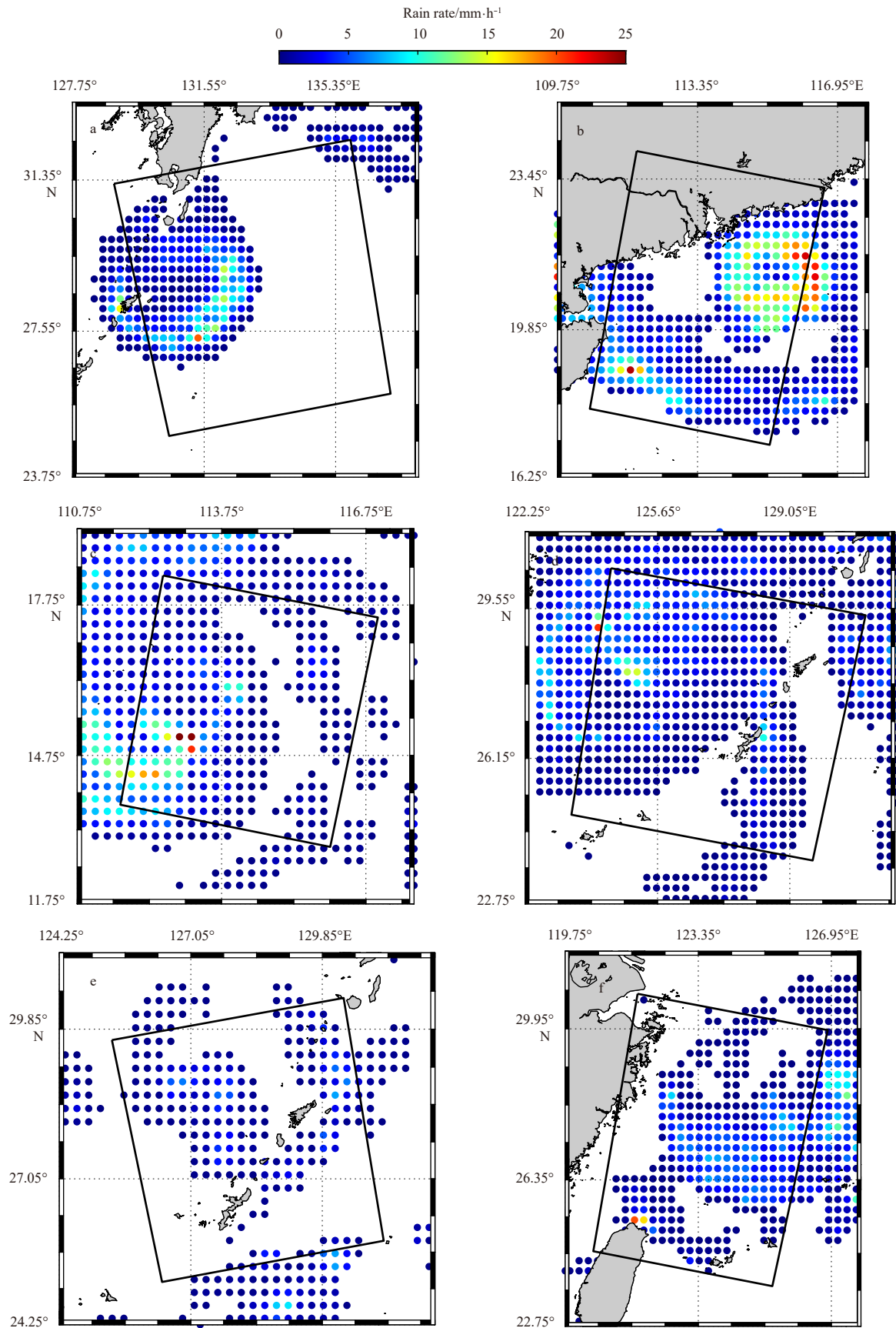


Fig. 3. The TRMM rainfall maps, in which the black rectangles in (a) to (f) correspond to the spatial coverage of six GF-3 SAR images as shown in Fig. 1.

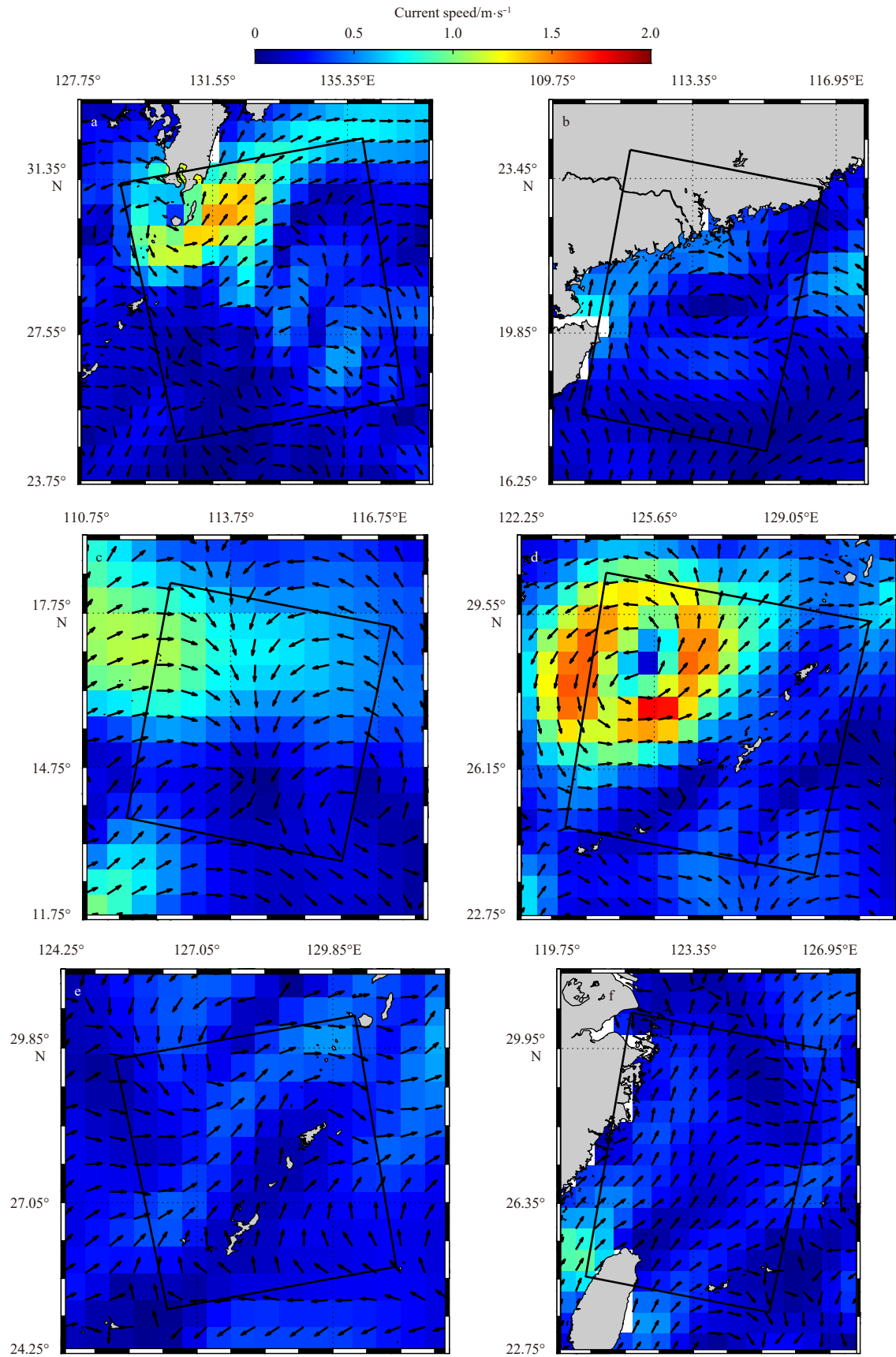


Fig. 4. The CFSv2 current maps, in which the black rectangles correspond to the spatial coverage of six GF-3 SAR images as shown in Fig. 1.

used. Another method is to use the composite surface model to segment the sea surface scale, which is still regarded as having a Gaussian distribution in each part, whereby only the partial wave spectra are changed by the tilting and hydrodynamic modulation effect of large and intermediate waves.

Each local scattering can be divided into three scattering components: large, intermediate and small. These three components are all related to the local incident angle and wave spectrum, and are affected by the tilt modulation and hydrodynamic modulation of the sea surface. Therefore, the sea surface needs to be divided into three kinds of scale grid.

In a radar resolution unit, large-scale and medium-scale scattering can be considered as invariant. Therefore, the scattering value can be averaged as follows:

$$\langle \sigma_{qp} \rangle = \langle \sigma_{qp}^l \rangle + \langle \sigma_{qp}^i \rangle + \langle \sigma_{qp}^s \rangle. \quad (10)$$

Small scale scattering can be expressed as

$$\sigma_{qp}^s(\mathbf{x}) \approx T(Z_x, Z_y) W(\mathbf{k}_H - \mathbf{k}_{sH}), \quad (11)$$

among $T(Z_x, Z_y) = \sqrt{1 + Z_x^2 + Z_y^2} \pi k^2 |\Gamma'_{qp}|^2 (k_{sz} - k_z)^2$, Z_x, Z_y is the slope of the x position, $\sqrt{1 + Z_x^2 + Z_y^2}$ is the area weighting factor after the local coordinates are tilted. The Γ'_{qp} is the polarization factor in the local coordinate system.

Suppose the Fourier expansion of wave height is

$$h(\mathbf{x}) = \int H(\mathbf{k}) \exp(i\mathbf{k} \cdot \mathbf{x}) + c.c. d\mathbf{k}, \quad (12)$$

where $H(\mathbf{k})$ is a wave height spectrum, and the relationship between $H(\mathbf{k})$ and spectrum $W(\mathbf{k})$ is satisfied as follows:

$$\langle H(\mathbf{k}_1) H^*(\mathbf{k}_2) \rangle = \begin{cases} \frac{1}{2} W(\mathbf{k}_1) & \mathbf{k}_1 = \mathbf{k}_2 \\ 0 & \mathbf{k}_1 \neq \mathbf{k}_2 \end{cases}. \quad (13)$$

Then the slope can be represented as

$$Z_x = \int i k_x H(\mathbf{k}) \exp(i\mathbf{k} \cdot \mathbf{x}) + c.c. d\mathbf{k},$$

$$Z_y = \int i k_y H(\mathbf{k}) \exp(i\mathbf{k} \cdot \mathbf{x}) + c.c. d\mathbf{k},$$

where $c.c.$ stands for the complex conjugate of the former term. By applying a Taylor expansion for Eq. (11), neglecting the high-order terms more than the cubic terms, and considering the hydrodynamics modulation of the Bragg spectrum by large and meso-scale waves we obtain:

$$\sigma_{qp}^s(\mathbf{x}) = T(0, 0) \left(1 + \frac{\partial T}{\partial Z_x} Z_x + \frac{\partial T}{\partial Z_y} Z_y + \frac{1}{2} \frac{\partial^2 T}{\partial Z_x^2} Z_x^2 + \frac{1}{2} \frac{\partial^2 T}{\partial Z_y^2} Z_y^2 + \frac{\partial^2 T}{\partial Z_x \partial Z_y} Z_x Z_y \right) \times$$

$$\left(1 + \int H(\mathbf{k}) T^h(\mathbf{k}) \exp(i\mathbf{k} \cdot \mathbf{x}) + c.c. d\mathbf{k} \right), \quad (14)$$

where $c.c.$ stands for the complex conjugate of the former term. σ_{qp}^s represents the Bragg scattering calculated with the average

gradient in a resolution unit and Bragg spectrum. $T^h(\mathbf{k})$ is the hydrodynamic modulation coefficient.

$$\langle \sigma_{qp}^s(\mathbf{x}) \rangle = \sigma_{qp0}^s + \int_{k_{res} < |\mathbf{k}| < k_s} \left\{ \text{Re} \left[i \left(\frac{\partial T}{\partial Z_x} k_x + \frac{\partial T}{\partial Z_y} k_y \right) H(\mathbf{k}) \right] + \frac{1}{2} \frac{\partial^2 T}{\partial Z_x^2} k_x^2 + \frac{1}{2} \frac{\partial^2 T}{\partial Z_y^2} k_y^2 + \frac{\partial^2 T}{\partial Z_x \partial Z_y} k_x k_y \right\} W(\mathbf{k}) d\mathbf{k}$$

$$= \sigma_{qp0}^s + \sigma_{qp2}^s, \quad (15)$$

where k_{res} is the wave number corresponding to the resolution unit, and k_s is the wavenumber corresponding to the small-scale grid. The second term σ_{qp2}^s on the right side of the formula represents the second order modulation of Bragg scattering due to waves with scales smaller than those of the radar resolution units.

Therefore, the scattering value of a resolution unit consists of four parts: the large, medium and small-scale scattering parts calculated by the average slope of the resolution unit, and the second order modulation of waves with scale smaller than the resolution unit.

$$\sigma_{qp} = \sigma_{qp}^l + \sigma_{qp}^i + \sigma_{qp0}^s + \sigma_{qp2}^s. \quad (16)$$

3.2 Simulated results

In order to obtain a reasonable dataset, the whole GF-3 SAR image is divided into a number of sub-scenes with a spatial coverage of about 10 km×10 km. These extracted sub-scenes cover the grids of ancillary data, e.g., ECMWF wind and wave, CFSv2 current and TRMM rainfall rate. In total, more than 1 000 matchups were available for our work. As shown in Fig. 5, a 0.8 correlation (COR) with a 2.89 dB root mean square error (RMSE) between simulated results and observed NRCSs from GF-3 SAR images is achieved, although the effect of rainfall is ignored in the simulation process. Figure 6 shows the spatial distribution maps

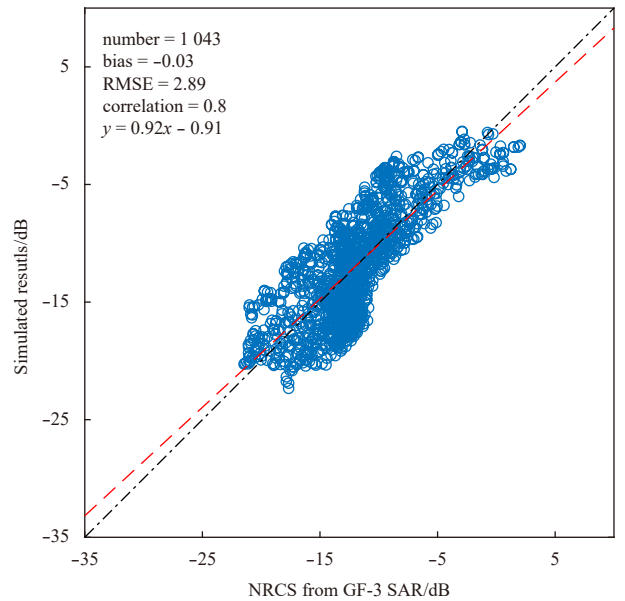


Fig. 5. The comparison between simulated results by using the method herein and NRCS of matchups from the collected GF-3 SAR images.

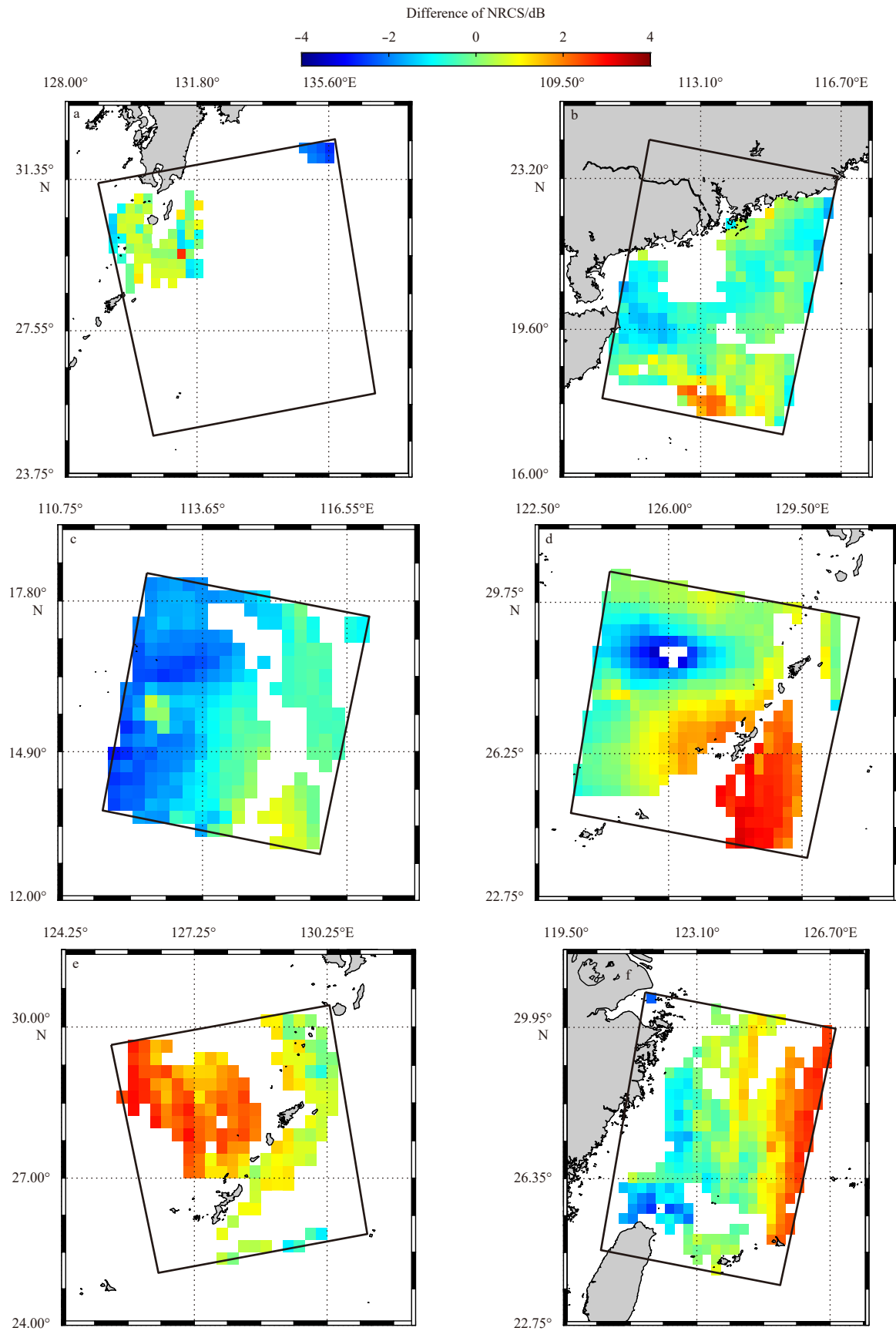


Fig. 6. The maps of difference between simulated NRCS and observed NRCS, in which the black rectangles correspond to the spatial coverage of six GF-3 SAR images as shown in Fig. 1.

of the difference of NRCS at the occurs of rainfall. It is roughly found that difference of NRCS grows with the increasing rainfall rate and this kind of behavior is clearly observed in Figs 6c and d corresponding to Typhoon Doksuri and Typhoon Talim. Under this circumstance, we consider the simulated results are suitable for analyzing the dependence of rainfall on GF-3 SAR to some extent, although the inherent error is included in the dataset.

4 Results and analysis

As mentioned in the introduction, the effect of the modification of sea roughness by rain on SAR data is a complicated mechanism. This includes the atmospheric attenuation and backscattering, which is separate from the surface rain effects and is not due to the coarse resolution of the collected GF-3 images, and the sea surface effects. A schematic diagram of the various surface effects on a SAR image caused by rainfall is illustrated in Fig. 7 (reproduced from Fig 1.1 in Long and Nie (2017)), in which raindrops striking the water create splash products in the splash area, rain-induced turbulence in the upper water layer is created in the damped wave area, the airflow of the down-draft roughens the sea surface, and the gust front is the outer edge of the downdraft. Using SAR-measured NRCS of GF-3 images in typhoons and collocated TRMM rain rate and ECMWF significant wave height, we quantitatively analyzed the different rain effects on GF-3 SAR acquired in GLO and WSC for different incidence angle ranges and sea states.

Figure 8 shows the relations between difference of NRCS and rainfall rate at various incidence angles, following the four meshes A to D as shown in Fig. 1. It seems that the difference of

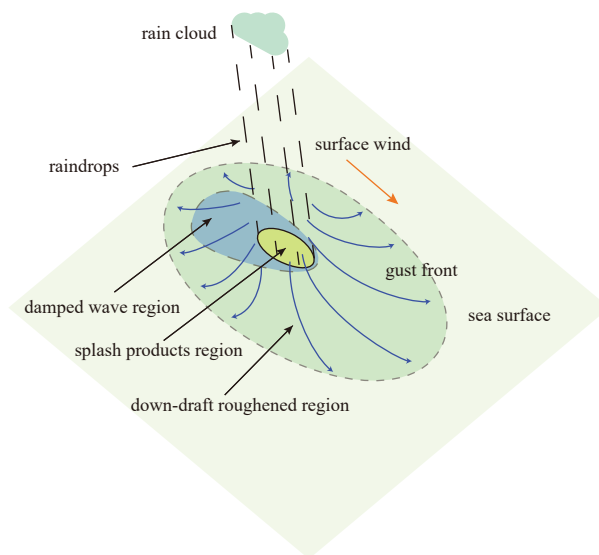


Fig. 7. The schematic diagram of the various surface effects on a SAR image caused by rainfall over the sea surface.

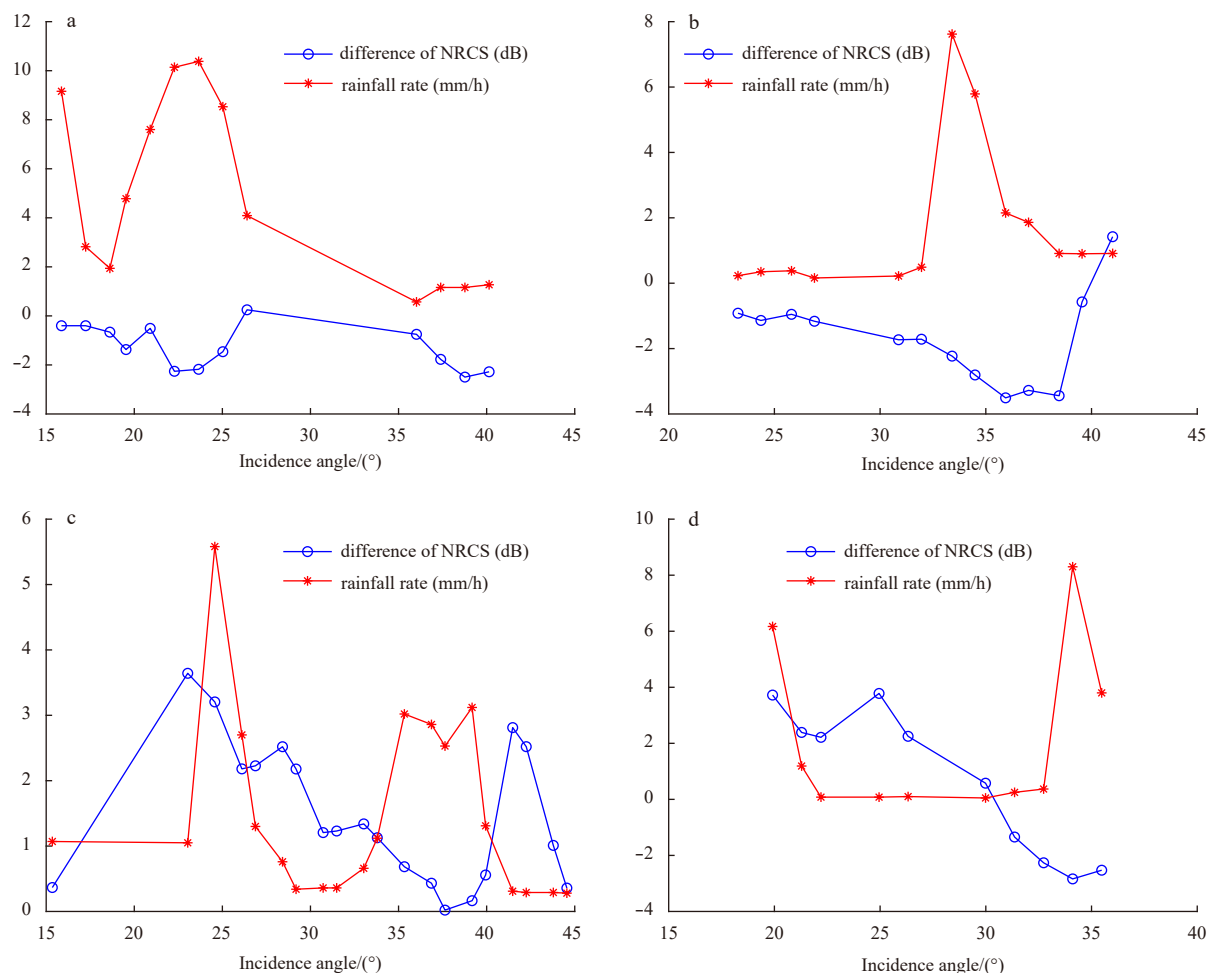


Fig. 8. The relations between difference of NRCS and rainfall rate at various incidence angles. (a) to (d) represents the four meshes A to D as shown in Fig. 1.

NRCS is related with rainfall rate to some extent. In particular, for the cases Typhoon Noru and Doksuri, the difference of NRCS increases with the increasing rainfall rate. Figure 9 shows the TRMM rainfall rate versus the difference between simulated NRCS and observed NRCS from the collected GF-3 SAR images, in which the colored lines represent the change of trend at various incidence angles ranging from 10° to 45° in 5° bins. It was found that the difference ranged from -4 dB to 4 dB and it can be clearly observed that the difference of NRCS is positive and decreases with the increasing rain rate at incidence angles from 15° to 30° . In contrast, the difference of NRCS is negative and increases with the increasing rain rate at incidence angles from 10° to 15° and from 30° to 45° . Generally, this behavior is consistent with the findings in Melsheimer et al. (2001), indicating that the effects of rain on SAR have a damping effect at low to moderate incidence angles and enhancement at high incidence angles. The exception is at incidence angles smaller than 15° because a non-Bragg reflection rather than the Bragg backscattering mechanism dominates at this condition.

5 Discussion

Similarly, Fig. 8 shows the WW3-simulated significant wave height versus the difference between simulated NRCS and SAR-measured NRCS. This is likely because rain damps the wave en-

ergy and rain-induced ring waves and down-draft may enhance the sea surface roughness. This is the probable explanation of the 'V' shape, shown by the black circles in Fig. 10. Although the theoretical-based algorithm Parameterized First-guess Spectrum Method (PFSM), can be applied for wave retrieval from S-1 SAR images in typhoons based on the good-quality SAR intensity spectrum (Ding et al., 2019), the inhomogeneous scenes, due to the presence of rain, are excluded in the retrieval process. This kind of behavior is worthy to be further studied through more SAR images in typhoon and hurricane.

6 Summary and conclusions

Rain retrieval is an interesting topic for the remote sensing community. With a fine horizontal resolution, e.g., 100 m to 1 km resolution compared to 12.5 km resolution for a scatterometer, SAR is a useful sensor for studying rain events, and this study focuses on investigating the performance of rainfall on GF-3 SAR in typhoons. The sea surface roughness on SAR is related quantitatively to capillary gravity waves, which can be affected by the atmospheric attenuation scattering of the radar signal generated by the falling rain. This in turn has an important influence on the retrieval of wind from SAR images (Ye et al., 2016).

Six GF-3 SAR images acquired in GLO and WSC mode were collected during the periods of Typhoon Noru, Doksuri, Talim,

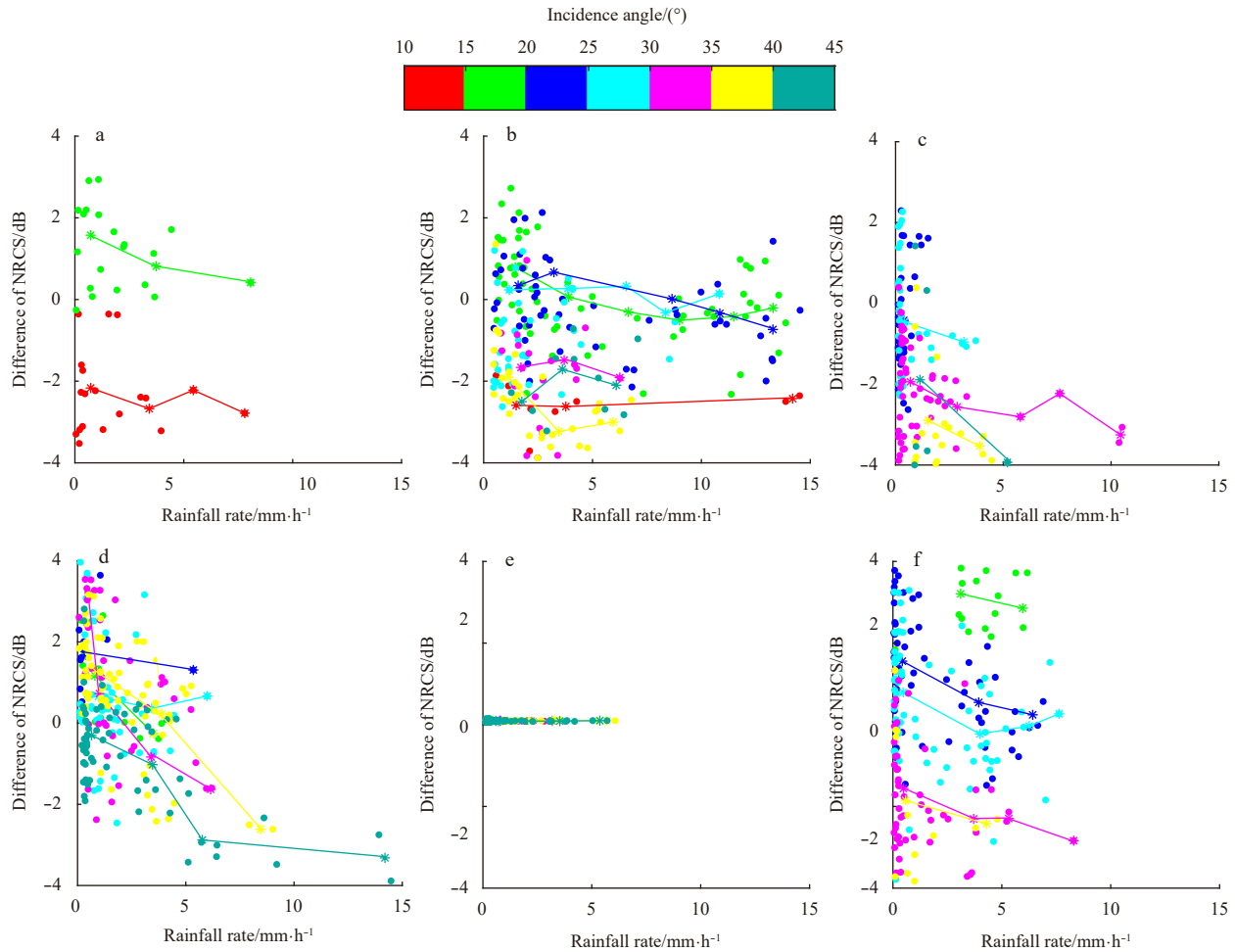


Fig. 9. The TRMM rainfall rate versus the difference between simulated NRCS and observed NRCS of matchups from the collected GF-3 SAR images, in which the colored lines represent the change of trend at various incidence angles ranging from 10° to 45° for a 5° bin. (a) to (f) represents results for the six cases as shown in Fig. 1.

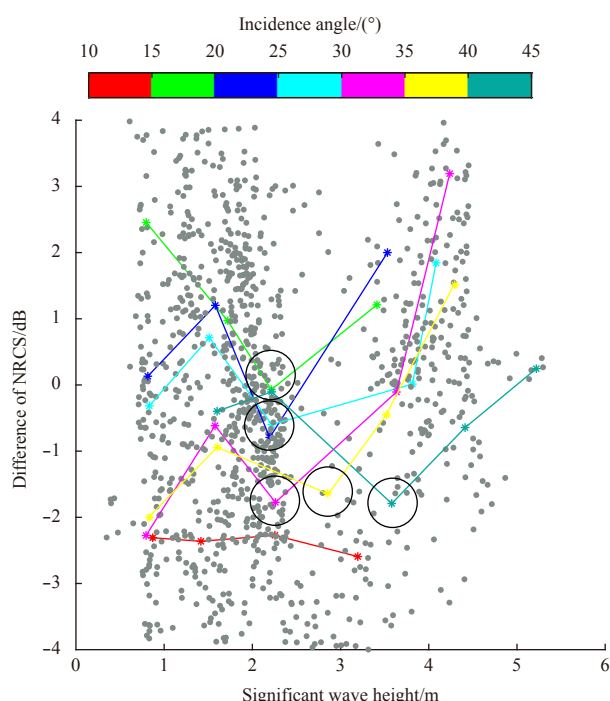


Fig. 10. The WW3-simulated significant wave height versus the difference between simulated NRCS and observed NRCS of matchups from the collected GF-3 SAR images, in which the colored lines represent the change of trend at various incidence angles ranging from 10° to 45° for a 5° bin.

Hato and Jongdari in 2017–2018, and the rain cells are visible in these C-band VV-polarization images. CFSv2 currents and ECMWF winds were collected for simulating NRCS using a parametric model. The dependences of the difference between model-simulated NRCS and SAR-measured NRCS on the TRMM rain rate and WW3-simulated significant wave height were analysed. The effects of rain signature vary with the incidence angle of the observations, having a damping effect on the SAR radar signal at incidence angles between 15° to 30° while enhancing the radar signal at incidence angles between 30° to 45° and incidence angles smaller than 10°. It was also found that the difference has a 'V' relationship with significant wave height at various incidence angles, therefore, including rain effects is important when attempting wave retrieval from SAR images.

In the near future, we will study the accuracy of wind and wave retrieval considering the rain-induced effects, and an algorithm for rain rate retrieval will be anticipated through more GF-3 SAR images in typhoons.

Acknowledgements

We appreciate the provision by the National Centers for Environmental Prediction (NCEP) of National Oceanic and Atmospheric Administration (NOAA) of the source code for the WAVEWATCH-III (WW3) model supplied free of charge. Gaofen-3 synthetic aperture radar (SAR) images are collected through an authorized account issued by the National Ocean Satellite Application Center (NSOAS) via <http://dds.nsoas.org.cn>. The European Centre for Medium-Range Weather Forecasts (ECMWF) data were accessed via <http://www.ecmwf.int>. Current field from the NCEP climate forecast system version 2 (CFSv2) is collected via <http://cfs.ncep.noaa.gov>. Rainfall data was collected from the

Tropical Rainfall Measuring Mission (TRMM) satellite via <ftp.trmmopen.gsfc.nasa.gov>. Typhoon parameters were provided by the Japan Meteorological Agency (JMA) via <http://www.jma.go.jp>.

References

- Allen J R, Long D G. 2005. An analysis of SeaWinds-based rain retrieval in severe weather events. *IEEE Transactions on Geoscience and Remote Sensing*, 43(12): 2870–2878, doi: [10.1109/TGRS.2005.858431](https://doi.org/10.1109/TGRS.2005.858431)
- Alpers W, Cheng C M, Shao Yun, et al. 2007. Study of rain events over the South China Sea by synergistic use of multi-sensor satellite and ground-based meteorological data. *Photogrammetric Engineering & Remote Sensing*, 73(3): 267–278
- Atlas D. 1994. Footprints of storms on the sea: A view from spaceborne synthetic aperture radar. *Journal of Geophysical Research: Oceans*, 99(C4): 7961–7969, doi: [10.1029/94JC00250](https://doi.org/10.1029/94JC00250)
- Cui Hong, He Hailun, Liu Xiaohui, et al. 2012. Effect of oceanic current on typhoon-wave modeling in the East China Sea. *Chinese Physics B*, 21(10): 109201, doi: [10.1088/1674-1056/21/10/109201](https://doi.org/10.1088/1674-1056/21/10/109201)
- Daper D W, Long D G. 2004. Evaluating the effect of rain on SeaWinds scatterometer measurements. *Journal of Geophysical Research: Oceans*, 109(C12): C02005, doi: [10.1029/2002JC001741](https://doi.org/10.1029/2002JC001741)
- Ding Yingying, Zuo Juncheng, Shao Weizeng, et al. 2019. Wave parameters retrieval for dual-polarization C-band synthetic aperture radar using a theoretical-based algorithm under cyclonic conditions. *Acta Oceanologica Sinica*, 38(5): 21–31, doi: [10.1007/s13131-019-1438-y](https://doi.org/10.1007/s13131-019-1438-y)
- Fritz J P, Chandrasekar V. 2012. A fully polarimetric characterization of the impact of precipitation on short wavelength synthetic aperture radar. *IEEE Transactions on Geoscience and Remote Sensing*, 50(5): 2037–2048, doi: [10.1109/TGRS.2011.2170576](https://doi.org/10.1109/TGRS.2011.2170576)
- Hallett J, Christensen L. 1984. Splash and penetration of drops in water. *Journal de Recherches Atmospheriques*, 18(4): 225–242
- Hersbach H, Stoffelen A, De Haan S. 2007. An improved C-band scatterometer ocean geophysical model function: CMOD5. *Journal of Geophysical Research: Oceans*, 112(C3): C03006, doi: [10.1029/2006JC003743](https://doi.org/10.1029/2006JC003743)
- Hersbach H. 2010. Comparison of C-band scatterometer CMOD5. N equivalent neutral winds with ECMWF. *Journal of Atmospheric and Oceanic Technology*, 27(4): 721–736, doi: [10.1175/2009JTECHO698.1](https://doi.org/10.1175/2009JTECHO698.1)
- Hwang P A, Zhang Biao, Toporkov J V, et al. 2010. Comparison of composite Bragg theory and quad-polarization radar backscatter from RADARSAT-2: with applications to wave breaking and high wind retrieval. *Journal of Geophysical Research: Oceans*, 115(C11): C08019, doi: [10.1029/2009JC005995](https://doi.org/10.1029/2009JC005995)
- Ji Qiyang, Shao Weizeng, Sheng Yexin, et al. 2018. A promising method of typhoon wave retrieval from Gaofen-3 synthetic aperture radar image in VV-polarization. *Sensors*, 18(7): 2064, doi: [10.3390/s18072064](https://doi.org/10.3390/s18072064)
- Kim J E, Alexander M J. 2013. Tropical precipitation variability and convectively coupled equatorial waves on submonthly time scales in reanalyses and TRMM. *Journal of Climate*, 26(10): 3013–3030, doi: [10.1175/JCLI-D-12-00353.1](https://doi.org/10.1175/JCLI-D-12-00353.1)
- Lin I I, Alpers W, Khoo V, et al. 2001. An ERS-1 synthetic aperture radar image of a tropical squall line compared with weather radar data. *IEEE Transactions on Geoscience and Remote Sensing*, 39(5): 937–945, doi: [10.1109/36.921411](https://doi.org/10.1109/36.921411)
- Long D G, Nie C. 2017. Hurricane precipitation observed by SAR. In: Li Xiaofeng, eds. *Hurricane Monitoring with Spaceborne Synthetic Aperture Radar*. Cham: Springer, 1–24.
- Masuko H, Okamoto K, Shimada M, et al. 1986. Measurement of microwave backscattering signatures of the ocean surface using X band and Ka band airborne scatterometers. *Journal of Geophysical Research: Oceans*, 91(C11): 13065–13083, doi: [10.1029/JC091iC11p13065](https://doi.org/10.1029/JC091iC11p13065)
- Melsheimer C, Alpers W, Gade M. 1998. Investigation of multifrequency/multipolarization radar signatures of rain cells over the

- ocean using SIR-C/X-SAR data. *Journal of Geophysical Research: Oceans*, 103(C9): 18867–18884, doi: [10.1029/98JC00779](https://doi.org/10.1029/98JC00779)
- Melshimer C, Alpers W, Gade M. 2001. Simultaneous observations of rain cells over the ocean by the synthetic aperture radar aboard the ERS satellites and by surface-based weather radars. *Journal of Geophysical Research: Atmospheres*, 106(C3): 4665–4677, doi: [10.1029/2000JC000263](https://doi.org/10.1029/2000JC000263)
- Nie Congling, Long D G. 2007. A C-band wind/rain backscatter model. *IEEE Transactions on Geoscience and Remote Sensing*, 45(3): 621–631, doi: [10.1109/TGRS.2006.888457](https://doi.org/10.1109/TGRS.2006.888457)
- Nie Congling, Long D G. 2008. A C-band scatterometer simultaneous wind/rain retrieval method. *IEEE Transactions on Geoscience and Remote Sensing*, 46(11): 3618–3631, doi: [10.1109/TGRS.2008.922146](https://doi.org/10.1109/TGRS.2008.922146)
- Nystuen J A. 1990. The underwater sound generated by light and heavy rain. *The Journal of the Acoustical Society of America*, 88(S1): S2, doi: [10.1121/1.2028946](https://doi.org/10.1121/1.2028946)
- Plant W J. 2002. A stochastic, multiscale model of microwave backscatter from the ocean. *Journal of Geophysical Research: Oceans*, 107(C9): 3120, doi: [10.1029/2001JC000909](https://doi.org/10.1029/2001JC000909)
- Ren Lin, Yang Jingsong, Mouche A, et al. 2017. Preliminary analysis of Chinese GF-3 SAR quad-polarization measurements to extract winds in each polarization. *Remote Sensing*, 9(12): 1215, doi: [10.3390/rs9121215](https://doi.org/10.3390/rs9121215)
- Romeiser R, Alpers W, Wismann V. 1997. An improved composite surface model for the radar backscattering cross section of the ocean surface: 1. Theory of the model and optimization/validation by scatterometer data. *Journal of Geophysical Research: Oceans*, 102(C11): 25237–237250, doi: [10.1029/97JC00190](https://doi.org/10.1029/97JC00190)
- Shao Weizeng, Sheng Yexin, Sun Jian. 2017a. Preliminary assessment of wind and wave retrieval from Chinese Gaofen-3 SAR imagery. *Sensors*, 17(8): 1705, doi: [10.3390/s17081705](https://doi.org/10.3390/s17081705)
- Shao Weizeng, Wang Jing, Li Xiaofeng, et al. 2017b. An empirical algorithm for wave retrieval from co-polarization X-band SAR imagery. *Remote Sensing*, 9(7): 711, doi: [10.3390/rs9070711](https://doi.org/10.3390/rs9070711)
- Shao Weizeng, Yuan Xinzhe, Sheng Yexin, et al. 2018. Development of wind speed retrieval from cross-polarization Chinese Gaofen-3 synthetic aperture radar in typhoons. *Sensors*, 18(2): 412, doi: [10.3390/s18020412](https://doi.org/10.3390/s18020412)
- Shao Weizeng, Zhu Shuai, Sun Jian, et al. 2019. Evaluation of wind retrieval from co-polarization Gaofen-3 SAR imagery around China Seas. *Journal of Ocean University of China*, 18(1): 80–92, doi: [10.1007/s11802-019-3779-8](https://doi.org/10.1007/s11802-019-3779-8)
- Sheng Yexin, Shao Weizeng, Zhu Shuai, et al. 2018. Validation of significant wave height retrieval from co-polarization Chinese Gaofen-3 SAR imagery using an improved algorithm. *Acta Oceanologica Sinica*, 37(6): 1–10, doi: [10.1007/s13131-018-1217-1](https://doi.org/10.1007/s13131-018-1217-1)
- Voronovich A G, Zavorotny V U. 2014. Full-polarization modeling of monostatic and bistatic radar scattering from a rough sea surface. *IEEE Transactions on Antennas and Propagation*, 62(3): 1362–1371, doi: [10.1109/TAP.2013.2295235](https://doi.org/10.1109/TAP.2013.2295235)
- Wang Lei, Han Bing, Yuan Xinzhe, et al. 2018. A preliminary analysis of wind retrieval, based on GF-3 wave mode data. *Sensors*, 18(5): 1604, doi: [10.3390/s18051604](https://doi.org/10.3390/s18051604)
- Weinman J A, Marzano F S, Plant W J, et al. 2009. Rainfall observation from X-band, space-borne, synthetic aperture radar. *Natural Hazards and Earth System Sciences*, 9(1): 77–84, doi: [10.5194/nhess-9-77-2009](https://doi.org/10.5194/nhess-9-77-2009)
- Xu Feng, Li Xiaofeng, Wang Peng, et al. 2015. A backscattering model of rainfall over rough sea surface for synthetic aperture radar. *IEEE Transactions on Geoscience and Remote Sensing*, 53(6): 3042–3054, doi: [10.1109/TGRS.2014.2367654](https://doi.org/10.1109/TGRS.2014.2367654)
- Ye Xiaomin, Lin Minseng, Yuan Xinzhe, et al. 2016. Satellite SAR observation of the sea surface wind field caused by rain cells. *Acta Oceanologica Sinica*, 35(9): 80–85, doi: [10.1007/s13131-016-0936-4](https://doi.org/10.1007/s13131-016-0936-4)
- Zhang Guosheng, Li Xiaofeng, Perrie W, et al. 2016. Rain effects on the hurricane observations over the ocean by C-band synthetic aperture radar. *Journal of Geophysical Research: Oceans*, 121(1): 14–26, doi: [10.1002/2015JC011044](https://doi.org/10.1002/2015JC011044)
- Zhu Shuai, Shao Weizeng, Armando M, et al. 2019. Evaluation of Chinese quad-polarization Gaofen-3 SAR wave mode data for significant wave height retrieval. *Canadian Journal of Remote Sensing*, 44(6): 588–600, doi: [10.1080/07038892.2019.1573136](https://doi.org/10.1080/07038892.2019.1573136)